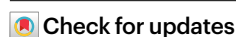


Homogeneous and mechanically stable solid–electrolyte interphase enabled by trioxane-modulated electrolytes for lithium metal batteries

Received: 19 September 2022

Accepted: 15 May 2023

Published online: 12 June 2023



Qian-Kui Zhang^{1,2,7}, Xue-Qiang Zhang^{1,2,7}, Jing Wan^{3,4}, Nan Yao⁵, Ting-Lu Song¹, Jin Xie⁵, Li-Peng Hou⁵, Ming-Yue Zhou⁵, Xiang Chen⁵, Bo-Quan Li^{1,2}, Rui Wen^{3,4}, Hong-Jie Peng⁶, Qiang Zhang⁵ & Jia-Qi Huang^{1,2}✉

The solid–electrolyte interphase (SEI) in lithium (Li) metal batteries is often heterogeneous, containing a diverse range of species and has poor mechanical stability. The SEI undergoes constant cracking and reconstruction during electrochemical cycling, which is accompanied by the exhaustion of active Li and electrolytes, hindering practical applications of the batteries. Here we propose an in situ structural design of SEI to promote its homogeneity and improve its mechanical stability. A bilayer structure of SEI is tailored through trioxane-modulated electrolytes: the inner layer is dominated by LiF to improve homogeneity while the outer layer contains Li polyoxymethylene to improve mechanical stability, synergistically leading to mitigated reconstruction of SEI and reversible Li plating/stripping. The coin cell consisting of an ultrathin Li metal anode (50 μm) and a high-loading cathode (3.0 mAh cm^{-2})—with the tailored bilayer SEI—achieves 430 cycles tested at 1.2 mA cm^{-2} , while the cell with an anion-derived SEI undergoes only 200 cycles under same conditions. A prototype 440 Wh kg^{-1} pouch cell (5.3 Ah), with a low negative/positive capacity ratio of 1.8 and lean electrolytes of 2.1 g Ah^{-1} , achieves 130 cycles.

In the pursuit of a net-zero society, rechargeable high-energy-density batteries are highly demanded to transform transportation and power sectors. However, the specific energy of state-of-the-art lithium (Li)-ion batteries based on the intercalation chemistry of graphite anodes is approaching the limit of 350 Wh kg^{-1} (refs. 1,2). The conversion chemistry of Li metal anodes, which could enable a battery with a specific

energy over 400 Wh kg^{-1} , is reviving for next-generation batteries³. Nevertheless, Li metal batteries suffer a short cycle life, severely hindering their practical applications⁴.

The short cycle life of Li metal batteries is usually a consequence of the rapid depletion of active Li and electrolytes^{4,5}, which is triggered by the continuous reactions between Li and electrolytes upon cycling^{6,7}.

¹School of Materials Science and Engineering, Beijing Institute of Technology, Beijing, China. ²Advanced Research Institute of Multidisciplinary Science, Beijing Institute of Technology, Beijing, China. ³Key Laboratory of Molecular Nanostructure and Nanotechnology and Beijing National Laboratory for Molecular Sciences, CAS Research/Education Center for Excellence in Molecular Sciences, Institute of Chemistry, Chinese Academy of Sciences, Beijing, China. ⁴University of Chinese Academy of Sciences, Beijing, China. ⁵Beijing Key Laboratory of Green Chemical, Reaction Engineering and Technology, Department of Chemical Engineering, Tsinghua University, Beijing, China. ⁶Institute of Fundamental and Frontier Sciences, University of Electronic Science and Technology of China, Chengdu, China. ⁷These authors contributed equally: Qian-Kui Zhang, Xue-Qiang Zhang. ✉e-mail: [jqhuang@bit.edu.cn](mailto:jquang@bit.edu.cn)

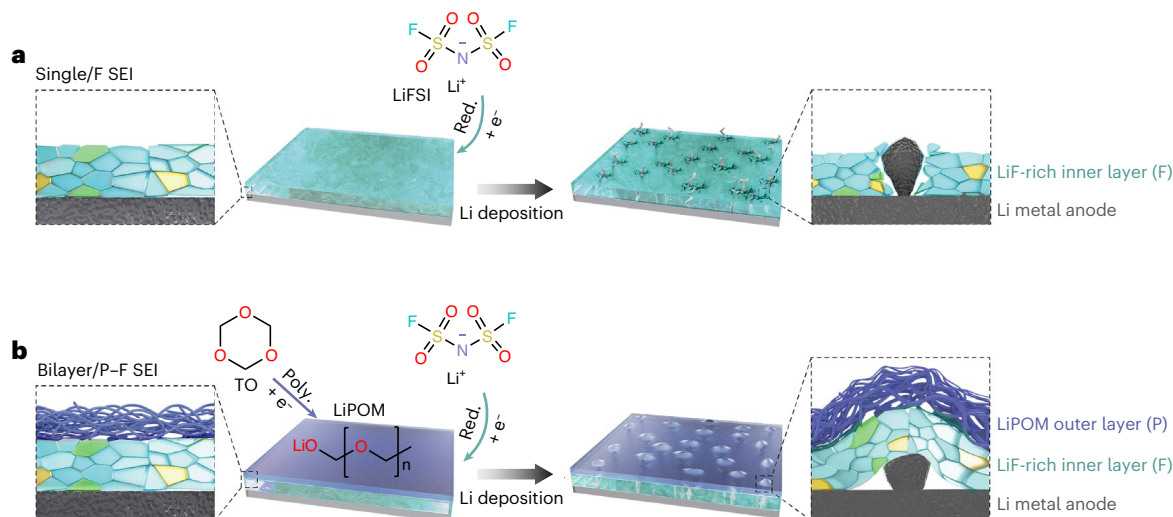


Fig. 1 | Schematic diagram of the structural evolution of single-layer and tailored bilayer SEIs during Li plating. **a**, Single/F SEI represents a single LiF-rich layer (abbreviated as F), which is derived from DME-based electrolyte composed of LiFSI:DME:HFE = 1.00:1.80:2.00 (by mol). Single/F SEI is fragile during Li plating. Red. represents the reduction of LiFSI. **b**, Bilayer/P-F SEI has

a homogeneous LiF-rich inner layer and a mechanically stable LiPOM outer layer (abbreviated as P), which is formed in TO-based electrolyte composed of LiFSI:TO:DME:HFE = 1.00:0.16:1.80:2.00 (by mol), exhibiting excellent tolerance to the volumetric deformation. Poly. represents the polymerization of TO.

Solid–electrolyte interphase (SEI) as a passivation layer in nanoscale thickness between Li and electrolytes can terminate such reactions and allow Li ions to diffuse through⁸. However, SEI derived from common organic electrolytes is heterogeneous and has poor mechanical stability^{9,10}. The heterogeneity of SEI results in spatially non-uniform Li-ion fluxes, further inducing uneven Li plating/stripping¹¹. Meanwhile, the poor mechanical stability of SEI facilitates its rupture due to the uneven stress distribution during the uneven Li plating/stripping that causes huge volume fluctuation^{12,13}, forming new hotspots for the spontaneous reactions between active Li and electrolytes. It is therefore pivotal to simultaneously improve the homogeneity and mechanical stability of SEI to mitigate the incessant reactions between Li and electrolytes for stabilizing Li metal anodes.

The homogeneity and mechanical stability of the SEI are sensitive to its components and structure^{14,15}. LiF^{16,17}, LiN_xO_y^{18,19} and Li₂O^{20,21} have been identified as the key components in dictating the homogeneity of SEI. In particular, the anion-derived and LiF-rich SEI, widely found in localized high-concentration electrolytes (LHCE), emerges as an effective route to improve the uniformity of SEI²². However, the single-layer, anion-derived SEI, which is composed of small LiF particles (single/F SEI)^{23,24}, is rather incompact with poor inter-particle connections and thus unsatisfactory mechanical stability to endure volume fluctuation (Fig. 1a). On the other hand, organic components in SEI are generally flexible to withstand moderate volumetric deformation. However, these components derived from common ether and carbonate solvents, including Li dicarbonates ((ROCO₂)₂Li), semicarbonates (ROCO₂Li), alkoxides (ROLi) and even oligomer, have insufficient mechanical strength and thus incline to break under extreme stress such as in against the extrusion of a Li dendrite^{15,25,26}. In both cases, the rupture of SEI is still not well mitigated. In addition to the components, the structure of SEI, that is, the arrangement of various components, is also crucial to regulate the homogeneity and mechanical stability^{14,27}. Generally, SEI displays a mosaic or a bilayer structure^{28,29}. A bilayer structure may avoid the mutual interference between the functions of various components in different layers furthest. Therefore, the nanoscale manipulation of SEI components and structure is essential to achieve the desirable homogeneity and mechanical stability of SEI.

Here we demonstrate an in situ structural design of SEI to enable desirable homogeneity and mechanical stability simultaneously and,

consequently, high-energy-density and long-cycling Li metal batteries. A bilayer structure of SEI, which consists of a LiF-rich inner layer that homogenizes Li-ion fluxes and an outer layer with Li polyoxymethylene (LiPOM) to improve mechanical stability, is in situ constructed in trioxane (TO)-modulated electrolyte (Fig. 1b). The tailored bilayer SEI is denoted as bilayer/P-F SEI, where bilayer describes the structure of SEI and P and F represent SEI components, that is, the outer polymer layer and the inner LiF-rich layer, respectively. The cracking and reconstruction of SEI in working batteries are substantially mitigated. Consequently, for coin cells of practical merits, such as high-loading LiNi_{0.5}Co_{0.2}Mn_{0.3}O₂ (NCM523) cathode (3.0 mAh cm⁻²) and ultrathin Li anode (50 μm), the lifespan is extended to 430 cycles tested at 1.2 mA cm⁻², significantly outperforming 200 cycles with routine anion-derived SEI. Furthermore, a Li metal pouch cell (5.3 Ah) achieves a high energy density of 440 Wh kg⁻¹ and delivers a lifespan of 130 cycles under a low negative/positive capacity ratio of 1.8 and lean electrolytes of 2.1 g Ah⁻¹.

In situ construction of the bilayer/P-F SEI

To construct the bilayer/P-F SEI, the electrolyte composed of Li bis(fluorosulfonyl)imide (LiFSI):TO:1,2-dimethoxyethane (DME):1,1,2,2-tetrafluoroethyl-2,2,3,3-tetrafluoropropylether (HFE) = 1.00:0.16:1.80:2.00 (by mol, denoted as TO-based electrolyte) is proposed, in which the molar ratio of TO is 3.2%. In TO-based electrolyte, LiFSI can generate a LiF-rich inner layer in SEI owing to significantly decreased free solvents (the low ratio between solvent and LiFSI), and TO is employed to form LiPOM in the outer layer due to its superior polymerizability³⁰. In contrast to Li alkyl carbonate, which severely deteriorates the homogeneity of SEI and the stability of Li metal batteries (Supplementary Fig. 1), LiPOM as a typical ROLi is conceived of displaying good compatibility with Li metal anodes³¹. Bilayer/P-F SEI is in situ constructed by the sequential reduction of LiFSI and TO in TO-based electrolyte as later revealed by experiments. A conventional LHCE constituting LiFSI:DME:HFE (1.00:1.80:2.00 by mol, denoted as DME-based electrolyte), which generates single/F SEI, is considered for comparison.

The polymerization mechanism of TO is investigated when TO is introduced into the electrolyte. In a mixed solvent of TO/DME, TO can polymerize upon contact with Li metal in the presence of Li

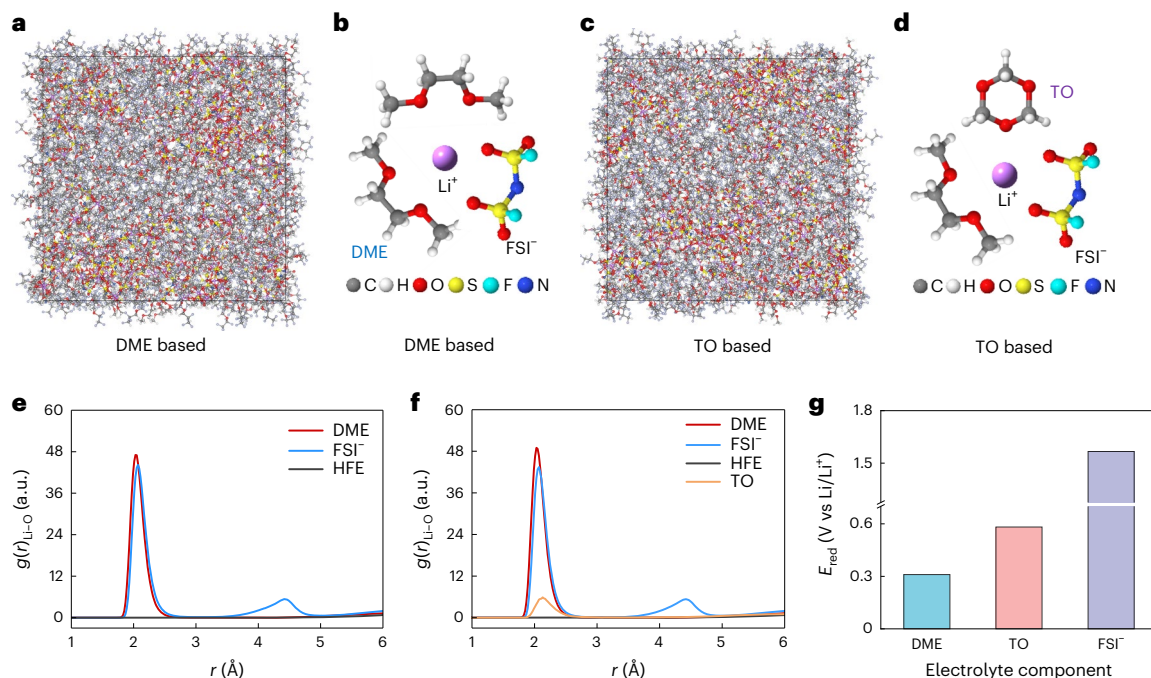


Fig. 2 | The solvation structure and reduction behaviour of DME- and TO-based electrolytes. a,c, Snapshots of the MD simulation boxes of DME- (a) and TO-based (c) electrolytes. The length of the side of the MD simulation cubic box is 56.5 and 56.9 Å for DME- and TO-based electrolytes, respectively. **b,d,** Schematic illustration of the representative solvation sheath of Li ions in DME- (b) and TO-based (d) electrolytes. Colours of elements: H, white; Li, pink; C, grey; N, blue;

O, red; F, cyan; S, yellow. **e,f,** The radial distribution function (RDF) plots of Li-O_{DME}, Li-O_{FSI}, Li-O_{HFE} and Li-O_{TO} pairs in DME- (e) and TO-based (f) electrolytes. **g,** The calculated reduction potential of DME, TO and FSI⁻ based on density functional theory. Y axis is broken for an easy comparison between DME and TO. The reduction potential of electrolyte components is abbreviated as E_{red} .

salts (Supplementary Fig. 2). It is deduced that the reduction of TO by Li metal initiates the polymerization, which is similar to the anionic ring-opening polymerization of 1,3-dioxolane as 1,3-dioxolane and TO are analogous cyclic ethers (Supplementary Fig. 3)³². According to gel permeation chromatography, TO-derived LiPOM has a high-number-average molecular weight (M_n) and a high-weight-average molecular weight (M_w) of 1.38×10^5 and 3.76×10^5 g mol⁻¹, respectively. The polymer dispersity index is about three, corresponding to a uniform molecular weight distribution. High-weight POM is characterized with high mechanical strength³³. Therefore, mechanical reinforcement by in situ formed LiPOM can be expected.

In addition to the polymerization capability, the solvation structure and the reduction behaviour of TO in the electrolytes play vital roles in generating SEI. Molecular dynamics (MD) simulations were carried out to investigate the solvation structure of both DME- and TO-based electrolytes (Fig. 2a–d, Supplementary Fig. 4 and Supplementary Fig. 5). TO can participate in the solvation sheath of Li ions in TO-based electrolytes (the peak of Li-O_{TO} at -2.1 Å). Meanwhile, both FSI⁻ and DME are involved in the solvation of Li ion in TO-based electrolytes as indicated by the two peaks corresponding to Li-O_{FSI} and Li-O_{DME} at -2.1 Å (Fig. 2e,f), which resembles the solvation structure of DME-based electrolyte, a typical electrolyte to form anion-derived SEI. Density functional theory calculations were then employed to quantify the reduction potential of DME, TO and FSI⁻ (Fig. 2g)^{34,35}. The reduction potential of TO (0.58 V) is higher than that of DME (0.31 V); while both are significantly lower than that of FSI⁻ (1.57 V). Consequently, FSI⁻ is preferentially reduced over TO and DME, leading to a LiF-rich inner layer of bilayer/P-F SEI; while TO is more inclined than DME to reduction, generating LiPOM in the outer layer.

The SEI structure was resolved by time-of-flight secondary ion mass spectrometry (ToF-SIMS). The ionic fragments of SEI components on the top surface (next to the electrolyte) are first detected (Supplementary Fig. 6 and Supplementary Fig. 7). LiF⁻ and C₂H₂O⁻ are

characteristic ionic fragments of LiF and organic components, respectively. LiF is abundant in both single/F SEI and bilayer/P-F SEI, but bilayer/P-F SEI contains more organic components than single/F SEI, implying that TO can decompose into LiPOM and involves the formation of SEI. The three-dimensional (3D) structure of SEI and spatial distribution of each component were further resolved by the depth profile analysis of ToF-SIMS (Fig. 3). As sputtering time increases, the content of LiF in both SEIs remains high while bilayer/P-F SEI is slightly LiF richer than single/F SEI further along the thickness (Fig. 3a–c). In contrast, there are organic components merely in the top layer of SEI, and their content decreases in both SEIs with the rise of sputtering time (Fig. 3a,b,d). However, the content of organic components in bilayer/P-F SEI is higher than that in single/F SEI, especially after 100 s of sputtering. Furthermore, the organic components in single/F SEI are too sparse in the lateral distribution to form a compact layer (Supplementary Fig. 8), and the organic components in bilayer/P-F SEI are compact to form a robust layer.

The above structure at the nanoscale was further confirmed by cryo-transmission electron microscopy (cryo-TEM). The bilayer/P-F SEI consists of an organic layer (outer layer) of 9 nm and an inorganic layer (inner layer) of 25 nm (Supplementary Fig. 9). In contrast, the single/F SEI is composed only of an inorganic layer of 40 nm. Note that the thickness of the inorganic layer in bilayer/P-F SEI is reduced by ~40%, which is conducive to reducing diffusion route length for uniform Li-ion fluxes, although the inorganic layer is dominated by LiF. It is inferred that the organic layer formed by TO as a barrier layer can hinder the inward diffusion of LiFSI towards Li metal anodes and then mitigate the continuous decomposition of LiFSI, therefore reducing the thickness of the inorganic layer. Meanwhile, the thickness of the organic layer in bilayer/P-F SEI is highly tunable by varying the molar ratio of TO in the electrolyte (Supplementary Fig. 10).

To analyse the composition of the organic layer, X-ray photoelectron spectroscopy (XPS) was employed with controlling sputtering

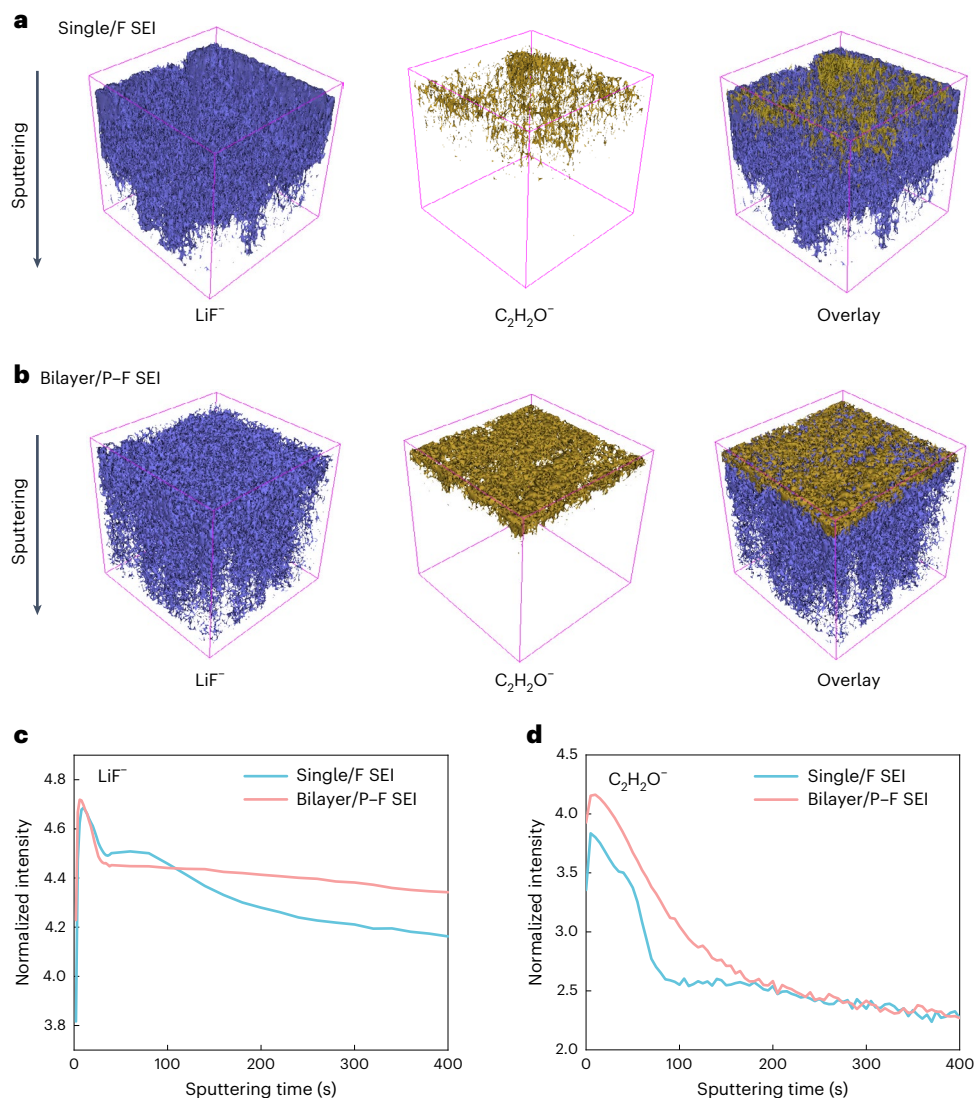


Fig. 3 | The 3D nanostructure of SEI resolved by ToF-SIMS. a,b, The 3D views of LiF⁻ (for LiF) and C₂H₂O⁻ (for organic components) in the ToF-SIMS sputtered volumes of single/F SEI (a) and bilayer/P-F SEI (b). **c,d,** The corresponding ToF-SIMS depth profiles for LiF⁻ (c) and C₂H₂O⁻ (d) in different SEIs. Normalized intensity is obtained through log (intensity) conversion.

time. In principle, the methylene-C bonded with two O atoms (O–C–O), as the basic unit of LiPOM, should exhibit higher C 1s binding energy than that of C atoms in DME and its derivatives (predominantly C–O). According to the fine fitting results of XPS C 1s spectra, bilayer/P-F SEI and single/F SEI exhibit more signals of O–C–O and C–O, respectively, revealing distinctive electrolyte decomposition pathways and products (Supplementary Fig. 11). The presence of O–C–O is attributed to TO-derived LiPOM while C–O to DME derivatives. Moreover, the atomic ratio of C in the bilayer/P-F SEI is 8.4 at.% (atomic ratio) higher than that in the single/F SEI at the sputtering time of 30s (Supplementary Fig. 12), aligning with the ToF-SIMS results. By combining the evidence from ToF-SIMS, cryo-TEM and XPS, we conclude that TO in the electrolyte enables the formation of a compact LiPOM-rich outer layer over the routine anion-derived SEI.

In situ measurement of mechanical stability of SEI

In situ electrochemical atomic force microscopy (AFM) is employed to probe the dynamic formation and mechanical stability of SEI in real-time. A specialized in situ electrochemical cell was designed where the Li wires are respectively used as the counter electrode and reference electrode, and the highly oriented pyrolytic graphite (HOPG) is

used as a working electrode (Fig. 4a). The typical topography of HOPG with atomically flat terraces and step edges at an open circuit potential (OCP) of 3.0 V is indicated in Fig. 4b. During the formation process of the single/F SEI, there are many tiny and irregular nanoparticles (about a dozen nanometres) below 1.11 V. These nanoparticles continue to grow until 0.74 V (Fig. 4c). The granular sediments increase to tens of nanometres and cover the surface of HOPG completely at 0.74 V (Fig. 4d). Meanwhile, there is no particle in other morphologies, which meets the expectation of a single/F SEI; these granular sediments are the decomposition products of FSI⁻ based on the calculated and reported reduction potential³⁶. When it comes to the bilayer/P-F SEI, nanoparticles in similar sizes and shapes to those for single/F SEI begin to appear below 1.06 V, a value again similar to that for single/F SEI (Fig. 4e,f). At 0.95 V, however, two different particles can be identified: porous but interconnected sediments (marked by the white circle) form over the granular substances (marked by the pink circles), as the interconnected sediments normally have higher height profiles in the AFM image. Given that these interconnected sediments appear later than the granular substances at a lower reduction potential, and the similarity between granular substances in both SEIs, the sequential reduction of FSI⁻ and TO to form bilayer/P-F SEI is confirmed.

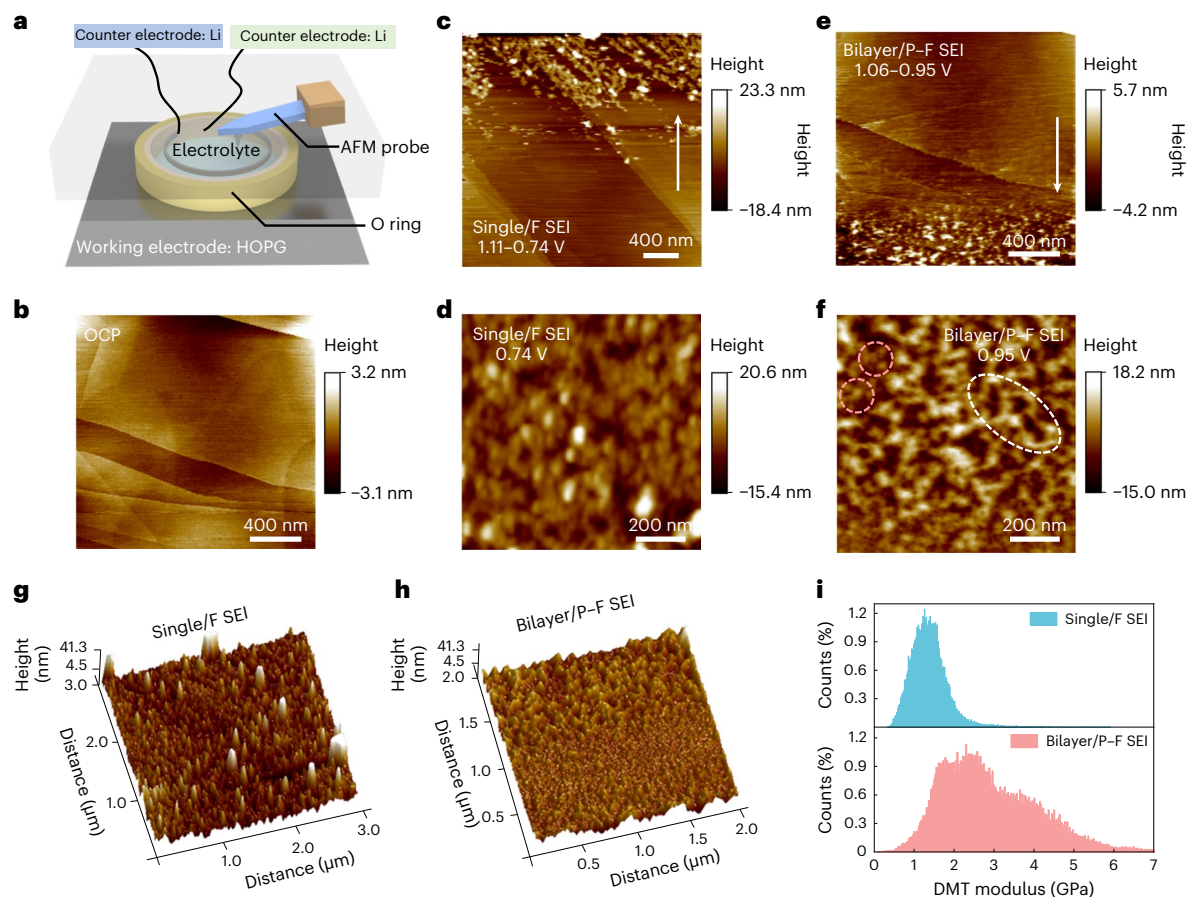


Fig. 4 | The formation process and mechanical stability of SEI resolved by in situ electrochemical AFM. **a**, Schematic illustration of the in situ electrochemical AFM cell. **b**, AFM topography images of HOPG at OCP (3.0 V). **c–f**, AFM topography images of single/F SEI (**c,d**) and bilayer/P-F SEI (**e,f**) upon

the cathodic scan of cyclic voltammetry. White arrows represent the scanning direction. **g,h**, The height image of single/F SEI (**g**) and bilayer/P-F SEI (**h**). **i**, DMT modulus distribution of single/F SEI and bilayer/P-F SEI.

The homogeneity and mechanical stability of SEIs were also investigated through AFM. The height of the single/F SEI concentrates in the range of 25–35 nm in a $3.0 \times 3.0 \mu\text{m}^2$ area for observation (Fig. 4g and Supplementary Fig. 13). However, the height of the bilayer/P-F SEI is mainly in the range of 10–22 nm (Fig. 4h and Supplementary Fig. 13). Not only is bilayer/P-F SEI thinner than single/F SEI, but also bilayer/P-F SEI possesses better homogeneity as indicated by the narrow distribution of height distribution. Derjaguin–Müller–Toporov (DMT) modulus was further measured by AFM to quantify the mechanical stability of SEI (Fig. 4i)^{37,38}. On the HOPG substrate, the average and maximum DMT moduli of bilayer/P-F SEI are 2.9 and ~6.5 GPa, respectively, both of which are ~2.1 times higher than those (average: 1.4 GPa; maximum: ~3.0 GPa) of single/F SEI. After Li deposition, the average DMT modulus of bilayer/P-F SEI on a working Li anode is 3.6 GPa, which is six times more than the DMT modulus (0.6 GPa) of single/F SEI (Supplementary Fig. 14a,b). In addition, the height distribution of deposited Li with bilayer/P-F SEI is more uniform than that with single/F SEI (Supplementary Fig. 14c–f). The force capable to pierce the SEI on deposited Li also confirms the enhanced mechanical stability of bilayer/P-F SEI (Supplementary Fig. 15). Via AFM-based nanoindentation method, force (F) versus displacement (d) curves recorded for single/F and bilayer/P-F SEIs reveal the force to pierce the SEI. The force curves indicate that a force of 211 nN applied by the AFM probe could pierce the single/F SEI, while a larger force of 439 nN is required to pierce the bilayer/P-F SEI. In short, the in situ electrochemical AFM characterization unravels that bilayer/P-F SEI has enhanced mechanical stability that can be well maintained under

working conditions, leading to superb durability to SEI rupture and improved uniformity of deposited Li.

Stabilized Li metal anode with bilayer/P-F SEI

The effect of the bilayer/P-F SEI on the reversibility of Li metal anodes was first evaluated by measuring the Coulombic efficiency (CE) of Li | Cu cells. The cell with bilayer/P-F SEI maintains a high CE (>99.5%) within 400 cycles at a current density of 1.0 mA cm^{-2} and a Li plating/stripping capacity of 1.0 mAh cm^{-2} , while the CE of the cell with single/F SEI fluctuates strongly after 270 cycles (Supplementary Fig. 16a). Even when the capacity increases to 3.0 mAh cm^{-2} , the cell with bilayer/P-F SEI maintains a high CE (>99.4%) within 100 cycles, outperforming that with single/F SEI (Supplementary Fig. 16b). Deposited Li in Li | Cu cells was subjected to detailed morphological analyses. During a single plating/stripping cycle, when compared with single/F SEI, bilayer/P-F SEI enables denser deposited Li with larger grains during Li plating and more uniform Li stripping that results in a compact residual film (Supplementary Fig. 17). After cycling, the stabilization effect of bilayer/P-F SEI over single/F SEI on Li deposition is also profound (Supplementary Fig. 18). The difference between Li deposition morphologies with the two SEIs well explains the distinct CEs of Li | Cu cells.

The effectiveness of bilayer/P-F SEI was evaluated in Li | NCM523 coin cells of practical merits, including ultrathin Li metal anodes ($50 \mu\text{m}$) and high-loading cathodes (3.0 mAh cm^{-2}). By defining cell lifespan as the cycle number where discharge capacity decays to 80% of the initial value, it is easily found that the cell with bilayer/P-F SEI exhibits a lifespan of 430 cycles, which is not only 115% longer than the

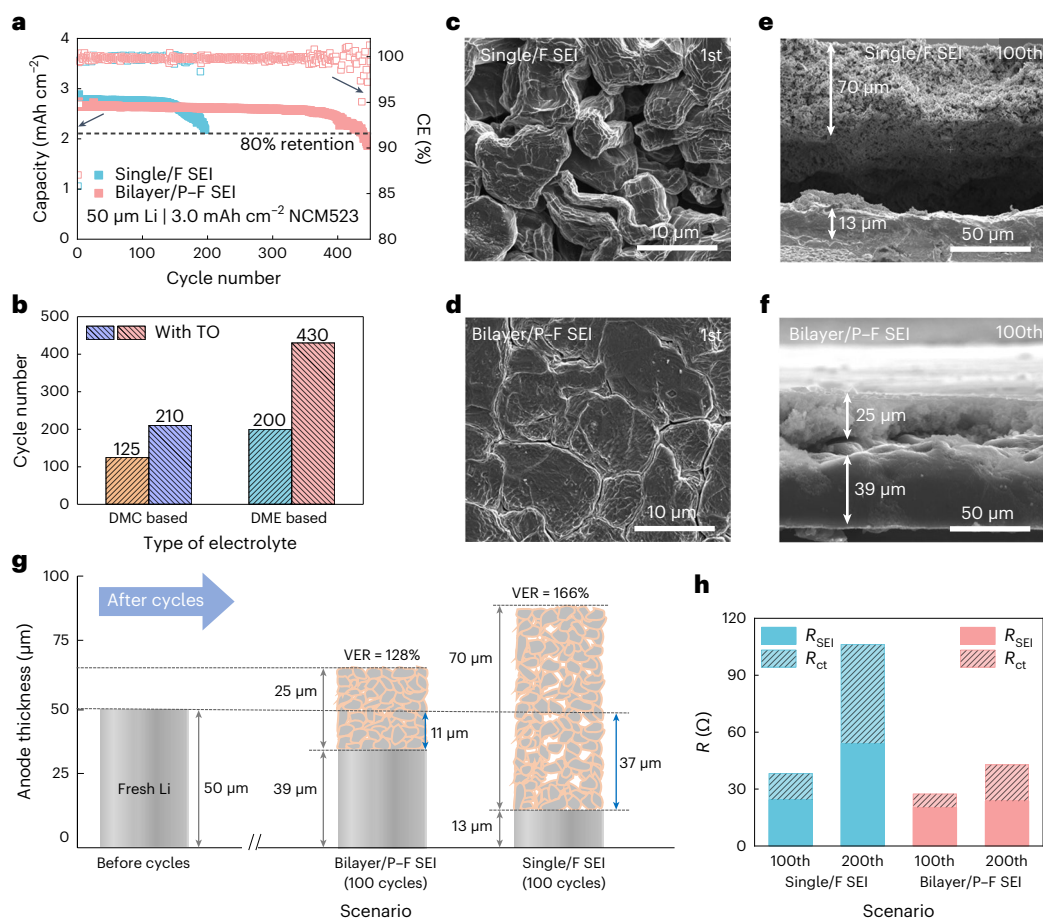


Fig. 5 | The effects of various SEIs on cycling stability of Li metal coin cells, Li morphology and interfacial kinetics. a, Cycling performance of Li | NCM523 coin cells with different SEIs at 0.4 C. **b**, Comparison of cycling performance of Li | NCM523 batteries with various electrolytes. **c–f**, Top-view and cross-sectional-view SEM images of Li metal anodes at the 1st and the 100th cycles

with single/F SEI (**c,e**) and bilayer/P-F SEI (**d,f**). **g**, Schematic illustration of anode evolution during cycling and the corresponding volume expansion after 100 cycles. X-axis is broken to make a clear distinction in the anode thickness before and after cycles. **h**, The evolution of interfacial resistance of Li | NCM523 coin cells after 100 and 200 cycles with single/F SEI and bilayer/P-F SEI.

cell with single/F SEI (200 cycles) (Fig. 5a) but also outstanding when compared with previous publications adopting similarly strict conditions such as thin anode ($\leq 50 \mu\text{m}$) and electrolyte lean ($\leq 50 \mu\text{l}$) (Supplementary Fig. 19). The great capacity decay of the cell with single/F SEI is accompanied by profound voltage polarization (Supplementary Fig. 20). Such a huge difference in cell lifespan resulted from the two SEIs is highly reproducible (Supplementary Fig. 21). The molar ratio of TO in the electrolyte also affects the cell lifespan, mainly by tuning the thickness of organic layer of bilayer/P-F SEI (as indicated by cryo-TEM), and a moderate thickness gives rise to the optimized lifespan (Supplementary Fig. 22). The bilayer/P-F SEI design can also work effectively when DME was replaced to dimethyl carbonate (DMC) (Fig. 5b and Supplementary Fig. 23). The lifespan of cells adopting DMC-based electrolytes is increased from 125 to 210 cycles when changing from single/F SEI to bilayer/P-F SEI.

The Li deposition morphology was investigated using scanning electron microscopy (SEM). The nucleation and initial growth behaviours of Li underneath the two SEIs are entirely different. With single/F SEI, the initial Li deposition is mostly whisker-like (Supplementary Fig. 24a–c), whereas with bilayer/P-F SEI, the initial Li deposition is pie-like with smooth edges (Supplementary Fig. 24d–f). Such a difference can be attributed to the improved homogeneity of bilayer/P-F SEI that guides uniform Li-ion transport across the SEI. Similar to the observation on Li | Cu cells, single/F SEI results in highly porous, nodule-like deposited Li ($\sim 9 \mu\text{m}$ in diameter, Fig. 5c). Bilayer/P-F SEI, however,

enables dense and large-grain ($\sim 15 \mu\text{m}$ in diameter) Li deposition, which is expected to alleviate electrolyte corrosion due to the reduced contact area (Fig. 5d). Minimizing such contact area is important to delay cell drying. After 200 cycles in Li | NCM523 cells, DME-based electrolyte is exhausted, but the TO-based electrolyte still has a surplus (Supplementary Fig. 25).

To quantify the evolution of Li anode from compact to porous (that is, from active to ‘dead’), the thickness of cycled Li was measured, and the volumetric expansion ratio (VER, the thickness of cycled Li divided by the thickness of fresh Li) was thereafter calculated. After 100 cycles, the cross-sectional SEM images show a sharp decrease in active Li (from 50 to 13 μm) and significant overall volume expansion of the Li anode (from 50 to 83 μm) with single/F SEI (Fig. 5e). In contrast, the thicknesses of active and dead Li with bilayer/P-F SEI are 39 and 25 μm , respectively (Fig. 5f). The calculated VERs with single/F and bilayer/P-F SEIs are 166% and 128%, highlighting the key role of bilayer/P-F SEI in mitigating formation of dead Li (by 64% after 100 cycles) and suppressing anode volume expansion (Fig. 5g). As the above volume expansion is shown to closely relate to dead Li accumulation, the accurate amount of Li loss was then determined through an electrochemical method (Supplementary Fig. 26). The Li loss after 200 cycles is 17% with bilayer/P-F SEI, which is nearly one-third of that with single/F SEI.

In addition, SEI is expected to tune Li interfacial kinetics, of which the evolution is often twined with the above morphological evolution. Electrochemical impedance spectroscopy of Li | NCM523 cells was

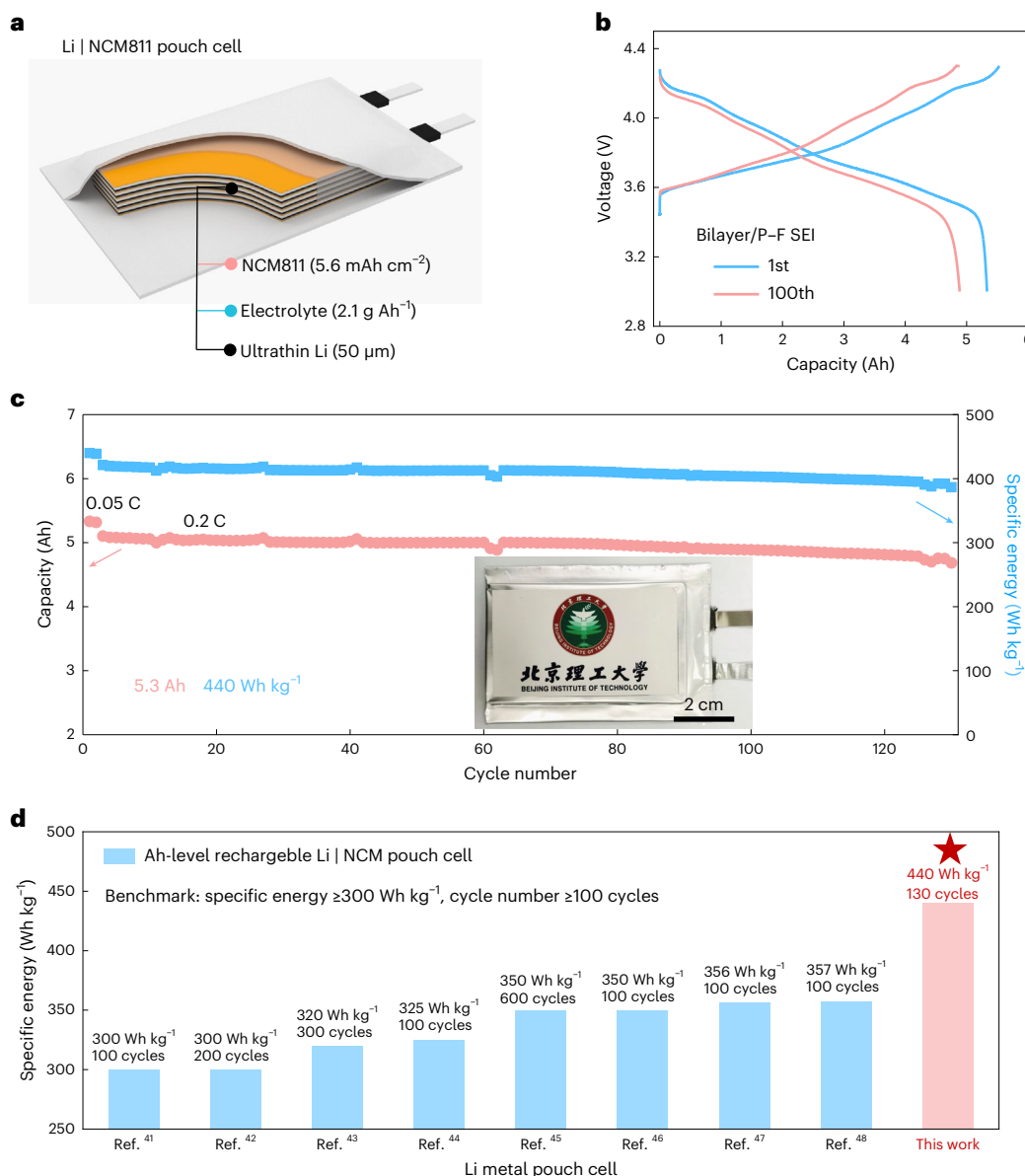


Fig. 6 | The performance of 440 Wh kg^{-1} Li metal pouch cells enabled by tailored bilayer SEI. a, Schematic illustration of a Li | NCM811 pouch cell of 440 Wh kg^{-1} . **b**, The voltage profiles of pouch cells at the 1st and the 100th cycles. **c**, Cycling performance of Li | NCM811 pouch cell at 0.1 C charge/0.2 C discharge

after two formation cycles at 0.05 C charge/discharge. The inset is the optical image of the corresponding pouch cell. **d**, The state-of-the-art performance of high-energy-density (over 300 Wh kg^{-1}) Li metal pouch cells with more than 100 cycles in published literature and this work.

analysed, where the semicircles in the high- and intermediate-frequency regions represent the resistance of SEI (R_{SEI}) and the charge transfer resistance (R_{ct}), respectively (Supplementary Fig. 27, Supplementary Table 1 and Supplementary Table 2). The total interface resistance, as a sum of R_{SEI} and R_{ct} , is denoted by R_{int} . With single/F SEI, R_{int} increases by 278% from the 100th cycle to the 200th cycle, much higher than the 120% increase in R_{int} with bilayer/P-F SEI (Fig. 5h). This is in agreement with the severe voltage polarization with single/F SEI (Supplementary Fig. 20). Notably, the change in R_{ct} is the main cause for the above increases with both two SEIs; but R_{SEI} with bilayer/P-F SEI is almost unchanged after cycles, in contrast to that with single/F SEI. Distribution of relaxation time analysis provides similar insights but in more detail (Supplementary Fig. 28)^{39,40}. The evolution of R_{ct} aligns with the dead Li accumulation. The drastic increase in R_{SEI} with single/F SEI is probably ascribed to SEI thickening because the lack of protection from a mechanically robust organic-rich shield results in continuous reactions that produce more SEI components. Therefore, the pivotal

role of SEI homogeneity and mechanical stability in regulating Li morphology and interfacial kinetics has been elucidated.

Bilayer/P-F SEI for practical Li metal pouch cells

Li | $\text{LiNi}_{0.8}\text{Co}_{0.1}\text{Mn}_{0.1}\text{O}_2$ (NCM811) pouch cells (5.3 Ah ; Fig. 6a and Supplementary Fig. 29) with lean electrolytes (2.1 g Ah^{-1}) and an ultra-low N/P ratio (the capacity ratio of negative electrode to positive electrode) of 1.8 were assembled and evaluated to demonstrate the effectiveness of bilayer/P-F SEI. The cell energy density is calculated by taking the masses of all components in pouch cells into consideration (Supplementary Table 3). Bilayer/P-F SEI enables the cell with a high retention of capacity and a low voltage polarization during cycling (Fig. 6b). The Li | NCM811 pouch cell achieves a specific energy of 440 Wh kg^{-1} at the cell level and maintains a capacity retention of 91.7% after 130 cycles at 0.1 C charge/0.2 C discharge (Fig. 6c). CE between the 1st and the 125th cycles is 99.7% on average, displaying a generally stable cycling trajectory (Supplementary Fig. 30). The thickness of pouch cell after 0, 70 and

130 cycles was recorded (Supplementary Fig. 31). The cell swelling rate is 18.6% at the 70th cycle, and 55.9% at the 130th cycle. Another pouch cell with an initial energy density of 435 Wh kg⁻¹ also achieves a capacity retention of 85.2% after 110 cycles at 0.1 C charge/discharge, demonstrating the reliability of bilayer/P–F SEI design at different cycling conditions (Supplementary Fig. 32). The specific energy achieved in this work (440 Wh kg⁻¹) is much higher than the state-of-the-art Li-ion batteries (250–270 Wh kg⁻¹). Furthermore, the performance of reported Li | NCM batteries is compared based on two criteria^{41–48}, including the cell-level energy density >300 Wh kg⁻¹ and the cycle life >100 cycles (Fig. 6d and Supplementary Fig. 33). Through the above comparison, the 130-cycle lifespan of Li metal batteries at a cell-level energy density of 440 Wh kg⁻¹ is superior, illustrating the extraordinary effectiveness of bilayer/P–F SEI in improving the anode stability in practical Li metal batteries. In addition, the techno economy and greenness of the electrolyte to generate bilayer/P–F SEI should be comprehensively analysed and considered in the future for the large-scale deployment of TO-based electrolytes or other LHCE analogues.

Conclusions

An in situ nanoscale structural design of bilayer/P–F SEI through rational electrolyte engineering is conceptualized and demonstrated to improve homogeneity and mechanical stability of SEI. The bilayer/P–F SEI consists of a LiF-rich inner layer to improve the homogeneity and an outer layer with LiPOM to improve the mechanical stability. Such a layered structure and the SEI formation mechanism via sequential reduction are resolved through a series of combinatorial characterization and theoretical tools such as cryo-TEM, in situ electrochemical AFM and MD. The improved homogeneity and mechanical stability of bilayer/P–F SEI leads to highly reversible Li plating/stripping with mitigated SEI reconstruction and prolonged lifespan of Li metal coin cells by 115% when compared with anion-derived SEI. In particular, a Li metal pouch cell of 440 Wh kg⁻¹ achieves a lifespan of 130 cycles. This work demonstrates a promising design of SEI for potential long-cycling and high-energy-density Li metal batteries. We expect that the design rationale can be exerted on other emerging battery systems.

Methods

Materials

Li foils (50 µm in thickness) were purchased from China Energy Lithium Co. Li foils were rolled on copper foils and then punched into discs with a diameter of 15.0 mm. DME (99.9% purity), DMC (99.9% purity), HFE (99.9% purity) and LiFSI (99.9% purity) were purchased from Suzhou Duoduo Chemical Technology Co. TO (>99% purity) was purchased from TCI Chemical Co. Battery-grade electrolyte, that is, 1.0 M hexafluorophosphate (LiPF₆) dissolved in fluoroethylene carbonate/DMC (1:4 by volume), was purchased from Suzhou Duoduo Chemical Technology Co. Polyethylene (PE) separator was purchased from Asahi Kasei Technosystem Co., and the diameter of PE separator is 19.0 mm in coin cells. LiNi_{0.5}Co_{0.2}Mn_{0.3}O₂ (NCM523, 3.0 mAh cm⁻²) cathode was bought from Guangdong Canrd New Energy Technology Co. and then was cut into discs with a diameter of 13.0 mm. LiNi_{0.8}Co_{0.1}Mn_{0.1}O₂ (NCM811) cathode with 5.6 mAh cm⁻² was purchased from Beijing WeLion New Energy Technology Co.

The preparation of electrolyte

The preparation of electrolyte was performed in an argon-filled glovebox with H₂O < 0.1 ppm and O₂ < 0.1 ppm. First, LiFSI was dissolved into DME, and then HFE was added to the above electrolyte to prepare a DME-based electrolyte. Next, TO was dissolved in DME-based electrolyte to prepare the TO-based electrolyte. The molar ratio of LiFSI, DME and HFE in DME-based electrolyte is 1.00:1.80:2.00. The molar ratio of LiFSI, TO, DME and HFE in the TO-based electrolyte is 1.00:0.16:1.80:2.00.

The preparation of coin cells

Li | NCM523 coin cells (2032 type) were assembled in an argon-filled glovebox with H₂O < 0.1 ppm and O₂ < 0.1 ppm. First, an Al foil (φ 19 mm) and then NCM cathode (with Al current collector) were placed in the cathode case and then 25 µl electrolyte was added to the surface of NCM cathode. Al foil can protect stainless steel can from corrosion and avoid the side effects at high voltage. Then, a PE separator was placed on the NCM cathode. Subsequently, 25 µl electrolyte was added to the surface of the PE separator. Then, Li metal anode with Cu current collector was placed on the PE separator, and Li metal anode faces the separator. Spacer, spring and anode case were put on the Cu current collector. Finally, the coin cell was sealed by a manual battery hydraulic sealer sealing machine with a pressure of 1,000 psi to enable close contact between each part.

The preparation of pouch cells

Li | NCM811 pouch cells (7.0 × 4.0 cm²) were assembled in a dry room at a dew point of –60 °C. The cathode is composed of aluminium current collector and double-layer active materials. The Li anode is composed of Cu current collector and double-layer Li foil. The thickness and mass loading of anode, cathode and other components are provided in Supplementary Table 3. First, the cathodes and anodes were stacked layer-by-layer with a PE separator (Supplementary Fig. 29). Second, nickel and aluminium cell tabs were welded to the Cu and aluminium current collector by ultrasonic spot welding, respectively, to connect with the battery cycler. Third, it was packed by aluminium plastic film with a specific size and a short-circuit detection was performed. Finally, the electrolyte was injected into the pouch cell, and the pouch cell was sealed.

Electrochemical tests

All coin cells were measured on a Neware battery cycler (CT-4008t) at 25 °C. Li | Cu cells were measured at a current density of 1.0 mA cm⁻² with a capacity of 1.0 or 3.0 mAh cm⁻². The Li | Cu cells were first discharged for 1.0 h or 3.0 h, then charged to the cut-off voltage of 1.0 V. Li | NCM523 cells were cycled in the voltage range of 3.0–4.3 V at 0.1 C for the initial two activation cycles and then at 0.4 C for the subsequent cycles (1.0 C = 180 mAh g⁻¹). Pouch cells were cycled in the voltage range of 3.0–4.3 V at 0.05 C for the initial three activation cycles and then at 0.1 C or 0.2 C for the subsequent cycles (1.0 C = 200 mAh g⁻¹). The cycling performance of the pouch cells was tested under a fixing device to provide 1.0 MPa external pressure. Electrochemical impedance spectroscopy of Li | NCM523 batteries (at the end of the charge) was conducted on a Solartron 1470E electrochemical workstation with a frequency from 10⁵–10⁻¹ Hz at an amplitude of 10 mV.

Material characterizations

The cycled Li | Cu and Li | NCM523 cells were disassembled in the Ar-filled glovebox, and Cu electrode (or Li electrode) was recollected followed by washing three times with DME solvents to remove the residual electrolyte. Li deposition morphology of Li | Cu cells and Li | NCM523 cells was characterized by SEM at 5.0 kV (FEI-APREO, Thermo Fisher Scientific). XPS (Kratos Analytical, Axis Supra+) was conducted to investigate the SEI components on Li metal anodes. The depth profiles were acquired via Ar⁺ sputtering at 2 kV for 0, 30 and 60 s. ToF-SIMS (PHI nano ToF II, ULVAC-PHI) also investigated SEI components on Li metal anodes. A special transfer vessel, which can directly transfer the sample from the glovebox to the vacuum chamber of ToF-SIMS, was used during sample transfer without being exposed to ambient air. The sputter etching was performed using an Ar⁺ beam (3 kV 100 nA) to obtain a depth profile. The area of analysis is 100 µm × 100 µm, while the sputtering area is 400 µm × 400 µm. The gel permeation chromatography measurements (1260 Infinity II, Agilent Technologies) were performed by dissolving the polymerization product in tetrahydrofuran. The morphology of SEI under high

resolution was recorded by a 2100 plus transmission electron microscope (TEM, JEOL Ltd.) working at 120 kV with an Elsa cryo-transfer station. Li metal was deposited on a Cu grid with a capacity of 0.5 mAh cm^{-2} deposited at 0.2 mA cm^{-2} . Then the Cu grid was soaked in DME. In the cryo-TEM test, Cu grid or microgrid was directly mounted to the holder (Gatan 698, cryo-transfer holder) and maintained at a low temperature of -170°C .

AFM characterization

A three-electrode system was employed in in situ electrochemical AFM experiments. HOPG is the working electrode, and Li wire is the counter and reference electrodes. Three electrodes were enclosed into a homemade electrochemical cell in the argon-filled glovebox with $\text{H}_2\text{O} < 0.1 \text{ ppm}$ and $\text{O}_2 < 0.1 \text{ ppm}$, and an O-type ring with a diameter of 15 mm was employed to seal the cell. The electrolytes are DME based and TO based. In situ electrochemical AFM experiments were performed in the glovebox by combining an electrochemical workstation (Methrohm Autolab, PGSTAT302N) with AFM (Bruker Corp., Dimension Icon). All potentials are referred to Li/Li^+ . The potential was negatively swept from OCP to the potential of SEI formation during charging process at the scan rate of 1 mV s^{-1} . AFM images were obtained by using an AFM probe (Bruker Corp., $f_0 = 300 \text{ kHz}$, $k = 26 \text{ N m}^{-1}$) to scan the surface of HOPG in the mode of PeakForce Quantitative Nano Mechanics (Peakforce QNM).

DFT calculations

The DFT calculations were conducted in Gaussian (G09) programme with B3LYP functional at 6-311 + G(d,p) level^{49,50}. The solvation model based on density (SMD) solvation model using parameters of DME was adopted to consider the solvation effect⁵¹. Frequency analysis was carried out to ensure the ground state of optimized ion–solvent complexes. The binding energy (E_b) between solvent molecules (DME or TO) with Li salt was defined as follows:

$$E_b = E_{\text{Li}^+-\text{FSI}^-\text{-solvent}} - E_{\text{Li}^+-\text{FSI}^-} - E_{\text{solvent}} \quad (1)$$

where $E_{\text{Li}^+-\text{FSI}^-\text{-solvent}}$, $E_{\text{Li}^+-\text{FSI}^-}$ and E_{solvent} represent the energy of the $\text{Li}^+-\text{FSI}^-\text{-solvent}$ cluster, Li^+-FSI^- salt and solvent, respectively.

The reduction potentials (E_{red}) of DME and TO were calculated based on the formula:

$$E_{\text{red}} = -\frac{G_{\text{red}} - G_{\text{init}} + \Delta G_{\text{solv}}^\circ(\text{red}) - \Delta G_{\text{solv}}^\circ(\text{init})}{F} - 1.4 \quad (2)$$

where G_{red} and G_{init} are the free energies of the reduced and initial $\text{Li}^+-\text{solvent}$ complexes in gas-phase at 298.15 K , respectively. $\Delta G_{\text{solv}}^\circ(\text{red})$ and $\Delta G_{\text{solv}}^\circ(\text{init})$ are the corresponding free energies of solvation. F is the Faraday constant, and the subtraction of 1.4 V accounts for the conversion to the Li/Li^+ potential scale.

MD simulations

MD simulations were performed using the Large Scale Atomic/Molecular Massively Parallel Simulator code^{52,53}. Two models containing 360 DME, 200 LiFSI and 400 HFE (total number of atoms: 14,960) or 360 DME, 200 LiFSI, 400 HFE and 32 TO molecules (total number of atoms: 15,344) were constructed. The parameters of DME and TO were obtained from optimized potentials for liquid simulations-all atom force field using LigParGen web server. The advanced restrained electrostatic potential (RESP2) atomic partial charges were used, which were generated by the Multiwfn programme based on electrostatic potential charges^{54,55}. The parameters of Li^+ and FSI^- were obtained from Jensen et al.⁵⁶ and Lopes et al.⁵⁷, respectively. The solvation structures were visualized by visualization for electronic and structural analysis⁵⁸. All three directions for all simulations use the periodic boundary conditions. Both van der Waals interactions and long-range correction (particle–particle particle mesh) of Coulombic interactions employ a

cut-off of 12 \AA . The fixed time step is 1 fs . All electrolyte models are first equilibrated in NPT ensemble (isobaric-isothermal ensemble) for 2 ns using the Parrinello–Rahman barostat to keep a pressure of 1 atm and a temperature of 298 K with time constants of 1 and 0.1 ps , respectively. Then, the electrolyte is heated from 298 to 420 K within 2 ns and kept at 420 K for 4 ns. After that, the models are annealed from 420 to 298 K within 2 ns and equilibrated at 298 K for another 4 ns in NPT ensemble (canonical ensemble). Finally, a 12 ns production run is conducted in NVT ensemble under a Nose–Hoover thermostat. Only the final 5 ns is adopted to analyse the radical distribution function, solvation structures and coordination number.

Data availability

The data supporting the findings of this study are available within the article and its supplementary information files.

References

1. Tarascon, J. M. & Armand, M. Issues and challenges facing rechargeable lithium batteries. *Nature* **414**, 359–367 (2001).
2. Winter, M., Barnett, B. & Xu, K. Before Li ion batteries. *Chem. Rev.* **118**, 11433–11456 (2018).
3. Cheng, X.-B. et al. Toward safe lithium metal anode in rechargeable batteries: a review. *Chem. Rev.* **117**, 10403–10473 (2017).
4. Louli, A. J. et al. Diagnosing and correcting anode-free cell failure via electrolyte and morphological analysis. *Nat. Energy* **5**, 693–702 (2020).
5. Zhou, M. Y. et al. Quantifying the apparent electron transfer number of electrolyte decomposition reactions in anode-free batteries. *Joule* **6**, 2122–2137 (2022).
6. Liu, J. et al. Pathways for practical high-energy long-cycling lithium metal batteries. *Nat. Energy* **4**, 180–186 (2019).
7. Chen, S. et al. Critical parameters for evaluating coin cells and pouch cells of rechargeable Li-metal batteries. *Joule* **3**, 1094–1105 (2019).
8. Peled, E. The electrochemical behavior of alkali and alkaline earth metals in nonaqueous battery systems—the solid electrolyte interphase model. *J. Electrochem. Soc.* **126**, 2047–2051 (1979).
9. Xu, K. Nonaqueous liquid electrolytes for lithium-based rechargeable batteries. *Chem. Rev.* **104**, 4303–4418 (2004).
10. Tikekar, M. D. et al. Design principles for electrolytes and interfaces for stable lithium-metal batteries. *Nat. Energy* **1**, 16114 (2016).
11. Lin, D., Liu, Y. & Cui, Y. Reviving the lithium metal anode for high-energy batteries. *Nat. Nanotechnol.* **12**, 194–206 (2017).
12. Yoon, I. et al. Measurement of mechanical and fracture properties of solid electrolyte interphase on lithium metal anodes in lithium ion batteries. *Energy Storage Mater.* **25**, 296–304 (2020).
13. Gao, Y. et al. Unraveling the mechanical origin of stable solid electrolyte interphase. *Joule* **5**, 1860–1872 (2021).
14. Li, Y. et al. Correlating structure and function of battery interphases at atomic resolution using cryoelectron microscopy. *Joule* **2**, 2167–2177 (2018).
15. Wang, W. W. et al. Evaluating solid-electrolyte interphases for lithium and lithium-free anodes from nanoindentation features. *Chem* **6**, 2728–2745 (2020).
16. Fan, X. et al. Non-flammable electrolyte enables Li-metal batteries with aggressive cathode chemistries. *Nat. Nanotechnol.* **13**, 715–722 (2018).
17. Zhang, X. Q. et al. Fluoroethylene carbonate additives to render uniform Li deposits in lithium metal batteries. *Adv. Funct. Mater.* **27**, 1605989 (2017).
18. Aurbach, D. et al. On the surface chemical aspects of very high energy density, rechargeable Li–sulfur batteries. *J. Electrochem. Soc.* **156**, A694–A702 (2009).

19. Liu, Y. et al. Solubility-mediated sustained release enabling nitrate additive in carbonate electrolytes for stable lithium metal anode. *Nat. Commun.* **9**, 3656 (2018).
20. Zhang, X. Q. et al. Highly stable lithium metal batteries enabled by regulating the solvation of lithium ions in nonaqueous electrolytes. *Angew. Chem. Int. Ed.* **57**, 5301–5305 (2018).
21. Ramasubramanian, A. et al. Lithium diffusion mechanism through solid–electrolyte interphase in rechargeable lithium batteries. *J. Phys. Chem. C* **123**, 10237–10245 (2019).
22. Chen, S. et al. High-voltage lithium-metal batteries enabled by localized high-concentration electrolytes. *Adv. Mater.* **30**, 1706102 (2018).
23. Wang, H. et al. Dual-solvent Li-ion solvation enables high-performance Li-metal batteries. *Adv. Mater.* **33**, 2008619 (2021).
24. Cao, X. et al. Monolithic solid–electrolyte interphases formed in fluorinated orthoformate-based electrolytes minimize Li depletion and pulverization. *Nat. Energy* **4**, 796–805 (2019).
25. Aurbach, D. Review of selected electrode–solution interactions which determine the performance of Li and Li ion batteries. *J. Power Sources* **89**, 206–218 (2000).
26. Zhang, Z. et al. Operando electrochemical atomic force microscopy of solid–electrolyte interphase formation on graphite anodes: the evolution of SEI morphology and mechanical properties. *ACS Appl. Mater. Interfaces* **12**, 35132–35141 (2020).
27. Gao, Y. & Zhang, B. Probing the mechanically stable solid electrolyte interphase and the implications in design strategies. *Adv. Mater.* **34**, e2205421 (2022).
28. Zhang, D. et al. Atomic-resolution transmission electron microscopy of electron beam-sensitive crystalline materials. *Science* **359**, 675–679 (2018).
29. Peled, E., Golodnitsky, D. & Ardel, G. Advanced model for solid electrolyte interphase electrodes in liquid and polymer electrolytes. *J. Electrochem. Soc.* **144**, L208–L210 (1997).
30. Weissmermel, K. et al. Polymerization of trioxane. *Angew. Chem. Int. Ed.* **6**, 526–533 (1967).
31. Xu, K. Electrolytes and interphases in Li-ion batteries and beyond. *Chem. Rev.* **114**, 11503–11618 (2014).
32. Aurbach, D., Youngman, O. & Dan, P. The electrochemical behavior of 1,3-dioxolane–LiClO₄ solutions—II. contaminated solutions. *Electrochim. Acta* **35**, 639–655 (1990).
33. Greene, J. P. in *Automotive Plastics and Composites* Ch. 8 (William Andrew Publishing, 2021).
34. Han, J. et al. Calculated reduction potentials of electrolyte species in lithium–sulfur batteries. *J. Phys. Chem. C* **124**, 20654–20670 (2020).
35. Wang, Y. et al. Theoretical studies to understand surface chemistry on carbon anodes for lithium-ion batteries: how does vinylene carbonate play its role as an electrolyte additive? *J. Am. Chem. Soc.* **124**, 4408–4421 (2002).
36. Zhang, X. Q. et al. Regulating anions in the solvation sheath of lithium ions for stable lithium metal batteries. *ACS Energy Lett.* **4**, 411–416 (2019).
37. Deng, X. et al. Morphology and modulus evolution of graphite anode in lithium ion battery: an in situ AFM investigation. *Sci. China Chem.* **57**, 178–183 (2014).
38. Zhang, Z. et al. Characterizing batteries by in situ electrochemical atomic force microscopy: a critical review. *Adv. Energy Mater.* **11**, 2101518 (2021).
39. Lu, Y. et al. The timescale identification decoupling complicated kinetic processes in lithium batteries. *Joule* **6**, 1172–1198 (2022).
40. Wan, T. H., Saccoccio, M., Chen, C. & Ciucci, F. Influence of the discretization methods on the distribution of relaxation times deconvolution: implementing radial basis functions with DRTtools. *Electrochim. Acta* **184**, 483–499 (2015).
41. Zhao, Q. et al. Upgrading carbonate electrolytes for ultra-stable practical lithium metal batteries. *Angew. Chem. Int. Ed.* **61**, e202116214 (2022).
42. Niu, C. et al. High-energy lithium metal pouch cells with limited anode swelling and long stable cycles. *Nat. Energy* **4**, 551–559 (2019).
43. Qiao, Y. et al. A high-energy-density and long-life initial-anode-free lithium battery enabled by a Li₂O sacrificial agent. *Nat. Energy* **6**, 653–662 (2021).
44. Gao, Y. et al. Effect of the supergravity on the formation and cycle life of non-aqueous lithium metal batteries. *Nat. Commun.* **13**, 5 (2022).
45. Niu, C. et al. Balancing interfacial reactions to achieve long cycle life in high-energy lithium metal batteries. *Nat. Energy* **6**, 723–732 (2021).
46. Zhang, L. et al. Practical 4.4 V Li||NCM811 batteries enabled by a thermal stable and HF free carbonate-based electrolyte. *Nano Energy* **96**, 107122 (2022).
47. He, B. et al. Scalable fabrication of a large-area lithium/graphene anode towards a long-life 350 Wh kg^{−1} lithium metal pouch cell. *J. Mater. Chem. A* **9**, 25558–25566 (2021).
48. Tang, Y. et al. Metal carbodiimides-derived organic–inorganic interface protective layer for practical high energy lithium metal batteries. *J. Power Sources* **536**, 231479 (2022).
49. Becke, A. D. Density-functional thermochemistry. III. the role of exact exchange. *J. Chem. Phys.* **98**, 5648–5652 (1993).
50. Frisch, M. J. et al. *Gaussian 09 Revision A.02* (Gaussian Inc., 2009).
51. Marenich, A. V., Cramer, C. J. & Truhlar, D. G. Universal solvation model based on solute electron density and on a continuum model of the solvent defined by the bulk dielectric constant and atomic surface tensions. *J. Phys. Chem. B* **113**, 6378–6396 (2009).
52. Steve, P. Fast parallel algorithms for short-range molecular-dynamics. *J. Comput. Phys.* **117**, 1–19 (1995).
53. Jorgensen, W. L., Maxwell, D. S. & Tirado-Rives, J. Development and testing of the OPLS all-atom force field on conformational energetics and properties of organic liquids. *J. Am. Chem. Soc.* **118**, 11225–11236 (1996).
54. Schauerl, M. et al. Non-bonded force field model with advanced restrained electrostatic potential charges (RESP2). *Commun. Chem.* **3**, 44 (2020).
55. Lu, T. & Chen, F.-W. Multiwfn: a multifunctional wavefunction analyzer. *J. Comput. Chem.* **33**, 580–592 (2012).
56. Jensen, K. P. & Jorgensen, W. L. Halide, ammonium, and alkali metal ion parameters for modeling aqueous solutions. *J. Chem. Theory Comput.* **2**, 1499–1509 (2006).
57. Canongia Lopes, J. N. et al. Potential energy landscape of bis(fluorosulfonyl)amide. *J. Phys. Chem. B* **112**, 9449–9455 (2008).
58. Momma, K. & Izumi, F. VESTA 3 for three-dimensional visualization of crystal, volumetric and morphology data. *J. Appl. Crystallogr.* **44**, 1272–1276 (2011).

Acknowledgements

J.-Q.H. acknowledges support by the National Key Research and Development Program (2021YFB2400300 and 2021YFB2500300) and Beijing Natural Science Foundation (JQ20004). X.-Q.Z. acknowledges support by the National Natural Science Foundation of China (22209010), China Postdoctoral Science Foundation (2021M700404) and Beijing Institute of Technology Research Fund Program for Young Scholars. X.C. acknowledges support by National Natural Science Foundation of China (22109086). We also acknowledge the support from Tsinghua National Laboratory for Information Science and Technology for theoretical simulations. We thank G.-X. Liu, J.-X. Tian, S.-Y. Sun, X.-Q. Ding and Y.-Q. Li for their helpful discussions.

Author contributions

J.-Q.H. and X.-Q.Z. conceived and designed the experiments. Q.-K.Z. assembled the coin cells and pouch cells. Q.-K.Z., X.-Q.Z., J.X., L.-P.H. and B.-Q.L. carried out material characterizations and electrochemical measurements. J.W. and R.W. performed in situ AFM characterization. T.-L.S. carried out the ToF-SIMS tests. N.Y. and X.C. performed the MD simulations. J.-Q.H. supervised this project. All authors engaged in result discussions. X.-Q.Z., M.-Y.Z., H.-J.P., Q.Z. and J.-Q.H. co-wrote the paper with input from all authors.

Competing interests

A patent related to the work has been submitted (application number CN202210942310.X) by Beijing Institute of Technology. The inventors are Jia-Qi Huang, Qian-Kui Zhang and Xue-Qiang Zhang. The patent refers to the methodology in this paper but provides more analogous additives than this work. The other authors declare no competing interests.

Additional information

Supplementary information The online version contains supplementary material available at <https://doi.org/10.1038/s41560-023-01275-y>.

Correspondence and requests for materials should be addressed to Jia-Qi Huang.

Peer review information *Nature Energy* thanks Chaojiang Niu and the other, anonymous, reviewer(s) for their contribution to the peer review of this work.

Reprints and permissions information is available at www.nature.com/reprints.

Publisher's note Springer Nature remains neutral with regard to jurisdictional claims in published maps and institutional affiliations.

Springer Nature or its licensor (e.g. a society or other partner) holds exclusive rights to this article under a publishing agreement with the author(s) or other rightsholder(s); author self-archiving of the accepted manuscript version of this article is solely governed by the terms of such publishing agreement and applicable law.

© The Author(s), under exclusive licence to Springer Nature Limited 2023